Repulsive three-body force and channel-coupling effects via ^{12}C + ^{12}C scattering at 100A MeV

W. W. Qu,[1,2,3,4] G. L. Zhang,[1,2,*] S. Terashima,[1,2] T. Furumoto,[5,6,†] Y. Ayyad,[7] Z. Q. Chen,[8] C. L. Guo,[1,2] A. Inoue,[7] X. Y. Le,[1,2] H. J. Ong,[7] D. Y. Pang,[1,2] H. Sakaguchi,[7] Y. Sakuragi,[9] B. H. Sun,[1,2] A. Tamii,[7] I. Tanihata,[1,2,7,‡] T. F. Wang,[1,2] R. Wada,[10] and Y. Yamamoto[11]

[1]*School of Physics and Nuclear Energy Engineering, Beihang University, Beijing 100191, China*
[2]*International Research Center for Nuclei and Particles in the Cosmos, Beihang University, Beijing 100191, China*
[3]*School of Radiation Medicine and Protection, Medical College of Soochow University, Soochow 215123, China*
[4]*Collaborative Innovation Center of Radiological Medicine of Jiangsu Higher Education Institutions, Soochow 215123, China*
[5]*Graduate School of Education, Yokohama National University, Yokohama 240-8501, Japan*
[6]*National Institute of Technology, Ichinoseki College, Ichinoseki, Iwate 021-8511, Japan*
[7]*Research Center for Nuclear Physics, Osaka University, Osaka 567-0047, Japan*
[8]*Institute of Modern Physics, Chinese Academy of Sciences, Lanzhou 730000, China*
[9]*Department of Physics, Osaka City University, Osaka 558-8585, Japan*
[10]*Cyclotron Institute, Texas A&M University, College Station, Texas 77843, USA*
[11]*RIKEN Nishina Center, Wako, Saitama 351-0198, Japan*

(Received 22 August 2016; revised manuscript received 3 February 2017; published 26 April 2017)

The angular distributions of differential cross sections of ^{12}C + ^{12}C elastic and inelastic scattering populating the ground and excited states in ^{12}C up to 15 MeV excitation energy are precisely measured for the first time at an incident energy of 100A MeV to study the effect of repulsive three-body forces. Using the high-resolution spectrometer Grand Raiden at the Research Center for Nuclear Physics (RCNP), Osaka University, we have obtained the differential cross sections for the ground state (0^+_1) and 4.44 MeV (2^+_1) excited state, as well as the summed differential cross sections for the states between 4.44 and 15 MeV in the angular range of 1.0°–7.5°. The results are compared with microscopic coupled-channel calculations. The potential between the colliding nuclei is determined by the double folding method with three different complex G-matrix interactions, the ESC, CEG07b, and MPa interactions. The CEG07b and MPa interactions, which include repulsive three-body forces, describe the data well, whereas the ESC interaction, which does not include repulsive three-body forces, fails to reproduce the data. The results provide evidence of repulsive three-body forces in ^{12}C and demonstrate the possible sensitivity of elastic scattering to three-body forces.

DOI: 10.1103/PhysRevC.95.044616

I. INTRODUCTION

Three-body forces (3BFs) are known to play an important role in the binding of nuclei and also in the equation of state (EOS) for nuclear matter. For the binding of nuclei, *ab initio* type calculations [1–5] that include the Fujita–Miyazawa interactions [6] have demonstrated the importance of the attractive 3BFs for understanding the structure of light nuclei. For the EOS, 3BFs are important for reproducing the saturation properties [7] and the compressibility at higher densities [8]. A high-density environment is produced by high-energy heavy-ion collisions so that sensitivity of the cross section to repulsive 3BFs is expected. In the present work, we study the relation between the high-energy ^{12}C + ^{12}C scattering cross sections and repulsive 3BFs.

Heavy-ion elastic scattering has been studied over a wide range of incident beam energies from 6A to 100A MeV, particularly for the ^{12}C + ^{12}C and ^{16}O + ^{16}O systems [9–11]. The availability of the experimental angular distributions of the differential cross sections has allowed the determination of the gross features of the local optical potentials and, in many cases, the unambiguous determination of the real parts of the potentials. The folding model is central to these studies and provides insight into the role of the realistic effective nucleon-nucleon (NN) interactions in determining nuclear structures [12]. The folding model for proton-nucleus elastic scattering has been successfully developed by applying the effective interactions from the complex G-matrix calculations including the 3BF effect in Refs. [13–15]. Using the same effective interactions, the double-folding model for heavy-ion collisions has also been developed, and the 3BF effect on the elastic and inelastic cross sections has been investigated [16–21]. However, it seems that the analysis of the scattering of heavy-ion systems with the confined 3BF effect provided by the chiral effective field theory (CEFT) does not include the medium effect in the high-density region, which has been shown to be important in Refs. [22,23]. Construction of a complex G-matrix interaction based on the CEFT interactions that takes into account the medium effect is thus anticipated. Nevertheless, all these theoretical studies show that the 3BF, in particular the repulsive component, has to be taken into account to explain the cross sections for high-energy collisions.

Recently, Furumoto *et al.* theoretically studied the effects of the repulsive 3BF in ^{12}C + ^{12}C and ^{16}O + ^{16}O elastic scattering at incident energies up to 400A MeV [18]. Clear

*zgl@buaa.edu.cn
†furumoto-takenori-py@ynu.ac.jp
‡tanihata@rcnp.osaka-u.ac.jp

effects of the 3BF in the differential cross sections for high-energy collisions were observed. The optical potential for heavy-ion collisions changes mostly in the real part with only a minor change observed in the imaginary part. At energies below 100A MeV the real part of the potential becomes shallower when the repulsive 3BFs are taken into account. Due to the short-range repulsion of the NN interactions, the real part of the optical potential becomes repulsive at an energy of 300A MeV without the 3BF. The inclusion of the repulsive 3BF adds a repulsive component to the potential and thus the real part of the optical potential becomes repulsive at lower energies, at around 200A MeV. Such a repulsive potential leads to the characteristic behavior of the diffraction pattern caused by the variation of the near-side and far-side components of the elastic cross section. Furumoto *et al.* therefore proposed observing the characteristic energy dependence of the differential cross sections for heavy-ion elastic scattering, which provides model-independent information on the change in the optical potential; in particular, the effect of repulsive forces.

The calculations of Furumoto *et al.* [18] also show the distinct effect of the repulsive 3BF on the differential cross sections at 100A MeV. Therefore, as a starting point for systematic experimental studies of the differential cross sections with different incident energies, we have measured elastic and inelastic scattering of $^{12}\mathrm{C} + {}^{12}\mathrm{C}$ at 100A MeV.

To completely understand elastic scattering, the effects of channel coupling must be considered. Previous data on elastic scatterings at 100A MeV [10,24,25] did not include data for related inelastic scattering, and thus a detailed comparison between the experimental data and theoretical calculations could not be made, including the channel coupling effect. In the present experiment, inelastic scattering cross sections for excitations up to 15 MeV have been measured precisely, together with the elastic cross section. In particular, the differential cross sections to the first-excited state, which gives the largest coupling effect, have been determined independently of the elastic and other inelastic channels.

A theoretical analysis of the data has been made by using the double folding method based on complex G-matrix interactions, which include the ESC, CEG07b [13,16], and MPa [26,27] models. The ESC interaction is based only on two-body NN interactions. The CEG07b interaction, on the other hand, includes the effective 3BF in addition to the two-body NN interactions. The repulsive part of the 3BF is expressed by the density-dependent change in the vector-meson masses, whereas the attractive part is based on the Fujita–Miyazawa diagram [6]. The MPa interaction also uses the 3BF, but the repulsive part is replaced by a multi-Pomeron exchange potential. Calculations have been performed within the framework of the microscopic coupled-channel calculations.

A part of this work has been previously published [21]. In this paper, we present the details of the data analysis method and refined cross sections. We also add new theoretical calculations and discussions. The following Sec. II describes the experimental procedure. The data analysis method and the results for the cross sections are presented in Sec. III. Section IV presents the theoretical methods. Comparisons between the results of the theoretical calculations and the experimental data are shown in Sec. V. The results are summarized in Sec. VI.

II. EXPERIMENTAL PROCEDURE

Elastic and inelastic scatterings for $^{12}\mathrm{C} + {}^{12}\mathrm{C}$ were measured at an incident energy of 100A MeV (1.2 GeV) at the Ring Cyclotron Facility of the Research Center of Nuclear Physics (RCNP) in Osaka University. The high-resolution spectrometer Grand Raiden was used for the measurements.

The $^{12}\mathrm{C}$ ions were produced by the NEOMAFIOS electron cyclotron resonance (ECR) ion source [28]. The ions generated in the ion source were injected into the azimuthally varying field (AVF) cyclotron accelerator with $K = 120$ (K is defined as acceleration voltage). The $^{12}\mathrm{C}$ beam was then injected into the ring cyclotron with six sectors with $K = 400$ [29] and accelerated up to 1.2 GeV. The accelerated beam was transported to the target position through the high-resolution west-south (WS) beam line [30]. The WS beam line was used to deliver a beam under a double achromatic condition. To obtain a small beam size and better angular resolution, a Monte Carlo method was used to simulate the beam condition on the target [31]. Based on the simulation we found a solution without collimation of the beam. A beam angular spread of 0.05° (1σ) or smaller was obtained under an achromatic focusing condition. The beam size was less than 2 mm at the target.

In this experiment the beam intensity was 0.1–1.0 particle nA on the target. A natural carbon target with a thickness of 1.18 mg/cm^2 was used for measurements at small scattering angles. A polyethylene film with a thickness of 11.40 mg/cm^2 was used as a thick target to obtain a higher yield at large angles. This target was also used for measuring $^{12}\mathrm{C} + p$ elastic scattering to calibrate and confirm the validity of the scattering angle and other analysis procedures. The obtained $^{12}\mathrm{C} + p$ elastic-scattering cross sections were compared with published data and the overall validity of the present measurement was confirmed.

The $^{12}\mathrm{C}$ particles scattered off the target were transported and analyzed by the Grand Raiden high-resolution magnetic spectrometer with excellent ion optical properties [32], illustrated in Fig. 1 (left). The position and angle of scattered $^{12}\mathrm{C}$ particles were measured by a detector system at the focal plane, also illustrated in Fig. 1 (right). The focal plane detectors were composed of two vertical drift chambers (VDC1 and VDC2) and three plastic scintillation detectors (PS1, PS2, and PS3) with thickness of 3, 10, and 10 mm, respectively. The scattered $^{12}\mathrm{C}$ particles were stopped in the PS3 detector. The two drift chambers VDC1 and VDC2 determined the trajectory of the scattered particles and the three plastic scintillation detectors determined the energy loss. Scattered $^{12}\mathrm{C}$ particles were identified from the two-dimensional correlation between the time-of-flight and the deposited energy in the plastic scintillators. The momentum of the scattered particles was determined by the horizontal position at the focal plane determined by VDC1 and VDC2 and the strength of the magnetic field. Coincidence signals from the two downstream scintillators PS1 and PS2 were taken as an event trigger. The

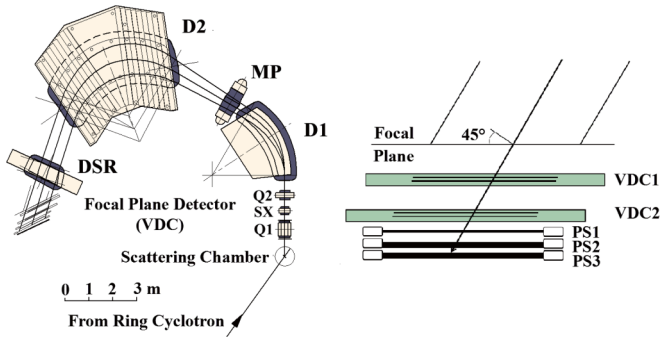

FIG. 1. Schematic view of the magnetic spectrometer Grand Raiden (left) and focal plane detector system setup (right). The spectrometer consists of two dipole magnets (D1 and D2), two quadrupoles (Q1 and Q2), a sextupole (SX), a multipole (MP), and an additional dipole (DSR) magnet.

PS3 detector was used to measure the residual energy of the scattered particles.

The laboratory scattering angle was from 1.0° to 7.5°. The horizontal and the vertical acceptances of the spectrometer were respectively set to ±20 mrad and ±6 mrad by the collimators placed at the entrance of the spectrometer. The central scattering angles of the Grand Raiden spectrometer were set to 2.0°, 2.5°, 3.5°, 5.0°, and 6.5° to guarantee overlap of the scattering angles between the different angular settings.

III. DATA ANALYSIS AND RESULTS

A. Particle identification and spectrum fitting

Particles were identified by the energy loss (ΔE)-time of flight (TOF) information obtained from the plastic scintillation detectors. The accelerator RF signal was used as the start signal in the TOF measurement. The particle identification results are shown in Fig. 2. The ^{12}C particles are clearly separated. Due to the thickness of PS2, a tail was found for the energy deposition by ^{12}C. The ^{12}C tail was precisely estimated by the shape of the ^{10}B and ^{12}C components. The ^{10}B component was subtracted from the one-dimensional histogram of the

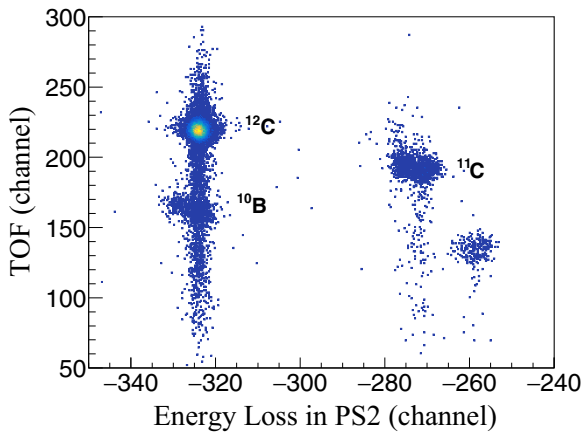

FIG. 2. Particle identification during ^{12}C + ^{12}C scattering experiment.

^{12}C energy-loss distribution in PS2. Through this method, the contribution of the tail was found to be less than (6.5 ± 0.5)% for all angles. However, the area selected for data analysis was only around the peak position. This event loss for ^{12}C was taken into account in the differential-cross-section calculation. Finally, the correction factor for the differential cross sections including the error was (6.5 ± 0.5)%.

For the reaction $A(a,b)B$, according to the energy and momentum conservations, we obtain the Q value for the reaction as

$$Q = K_b - K_a - m_B + \sqrt{m_B^2 + \tau}, \tag{1}$$

where $c = 1$ and

$$\tau = K_a^2 + 2K_a m_a + K_b^2 + 2K_b m_b - 2\sqrt{\left(K_a^2 + 2K_a m_a\right)\left(K_b^2 + 2K_b m_b\right)}\cos\theta. \tag{2}$$

The light velocity c is omitted as a natural unit. m_a, m_b, and m_B represent the masses of the projectile and the scattered and recoil nuclei, respectively. K_a and K_b respectively denote the kinetic energies of the projectile and the ejected particles, and θ is the scattering angle for the ejected particles in the laboratory frame. Using Eqs. (1) and (2), Q values were obtained event by event. The momentum of a scattered ^{12}C particle was obtained by adding the central setting momentum p_c of the spectrometer and momentum shift Δp obtained from the measured position at the focal plane ($p = p_c + \Delta p$).

The scattering angle θ was determined from the angle θ_d for the particle path at the focal plane, the central angle of the spectrometer and the measured angular shift from the center. The relation between θ and θ_d was obtained from the optical matrix for the spectrometer and confirmed by a sieve slit placed before the spectrometer. The vertical angles for the particles were not taken into account due to the limited vertical acceptance compared to the horizontal acceptance. A faint ^{12}C primary beam was used in an empty target run to determine the angular resolution to be 0.105° (full width at half maximum, FWHM) in the present experiment.

An example two-dimensional plot of the scattering angle and the excitation energy for ^{12}C is shown in Fig. 3. Three horizontal bands, which correspond to the ground state and the 4.44 MeV (2_1^+) and 9.64 MeV (3_1^-) excited states for ^{12}C + ^{12}C scattering, can be clearly seen. The curved band seen in the figure is due ^{12}C scattered from hydrogen in the target. From the kinematics calculation, the ^{12}C + p elastic scattering and the ^{12}C + ^{12}C to 4.44 MeV excitation cross at a scattering angle of 1.015° for the present energy. Another crossing with the focus of the 9.64 MeV excitation for ^{12}C + ^{12}C occurs at 1.5°. From Fig. 3, it is clearly observed that the crossing angles are consistent with the kinematics and are thus independent confirmation of the scattering angle determination. The contributions of hydrogen were subtracted by using previous data [33]. Details of the subtraction process have been previously described [34].

The two-dimensional plot in Fig. 3 was sliced into excitation energy spectra of different angles. The excitation energy spectra were analyzed for an angular step of 0.095°. An example slice at 1.5° is shown in Fig. 4. A peak at an

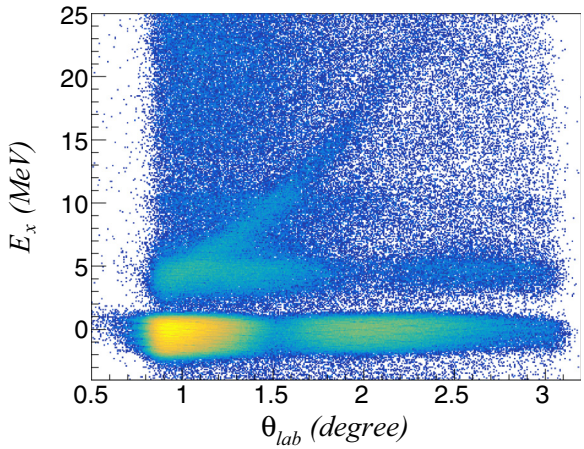

FIG. 3. Two-dimensional plot of excitation energy and laboratory angles for outgoing ^{12}C particles for the spectrometer central angle of 2.0°.

excitation energy of 0 MeV arises from the elastic scattering. The asymmetric shape of the peak is due to the asymmetric broadening of the incident beam energy. Therefore, we used this shape as the lineshape in the subsequent fitting process for the excited states.

The peak to the right of the ground-state peak represents inelastic scattering to the 4.44 MeV state (the first-excited state of ^{12}C). A shoulder observed on the right side of the peak is due to projectile excitation events. In the present experiment, the missing-mass technique does not distinguish the excitations for the target and the projectile. Due to the γ-decay recoil of the excited projectile, the original spectrum is modified and has a

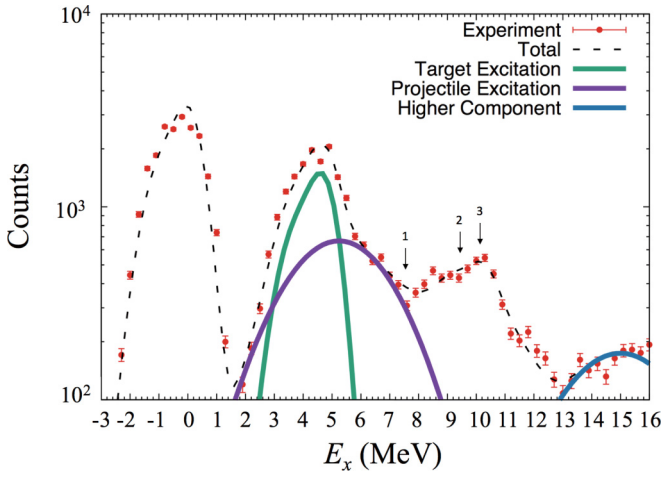

FIG. 4. Example excitation spectrum obtained at scattering angle of 1.5°. The horizontal and vertical axes represent excitation energy and counts, respectively. The fitted spectrum for the 4.44 MeV excited state with the target and projectile excitation components is shown. The spectral shape for the ground state is used as the lineshape. The red and green curves show the phenomenological components of the projectile and target excitations, respectively. The arrows numbered 1, 2, and 3 show the peak positions for the 7.65 MeV (0_2^+) state, the 9.64 MeV (3_1^-) state, and the 10.30 MeV state, respectively.

wider distribution. The modified spectral shape was calculated by assuming the isotropic emission of γ rays from the excited state. This spectrum was then folded by the lineshape used for data fitting. The obtained shape together with the lineshape determined for the ground state was used to fit the peak for the 4.44 MeV (2_1^+) state. The results are shown in Fig. 4. The two components for the 4.44 MeV (2_1^+) state are clearly seen. Up to this region of excitation energy, the peaks can be clearly separated. Moreover, the fitted values for the strength of these transitions are almost the same as the simple sum for the events at the peak regions.

The spectrum between 6 and 12 MeV was also fit by the same procedure. The fitting results are also shown in Fig. 4 assuming contributions from the 7.65 MeV (0_2^+), 9.64 MeV (3_1^-) and 10.30 MeV states and mutual excitation of the 4.44 MeV states. If the excitation energy is higher than 7.27 MeV, the ^{12}C* decays by emitting α particles. Therefore, no projectile excitations with an excitation energy higher than 7.27 MeV were detected in the present setup. The lineshape for the ground state was applied to the 7.65 MeV (0_2^+) state and the 9.64 MeV (3_1^-) states. For the 10.30 MeV state, a Gaussian function with a width of 3.07 MeV FWHM was used [35]. The mutual excitation peak is expected to appear at around 4.44 (Target) + 4.44 (Projectile) MeV. However, those events could not be estimated in the present work. Because of this ambiguity, even though the fittings for the 7.65 MeV (0_2^+) state, the 9.64 MeV (3_1^-) state and the 10.30 MeV state can well reproduce the excitation energy spectrum in some cases, these states cannot be separately observed for many scattering angles. Therefore, only the integrated cross sections for those states are presented in this paper.

For excitation energies higher than 12 MeV, there exist many excited states, and the resolution of the magnetic spectrometer is not sufficient to distinguish each component showing a continuum. The data above 12 MeV are not presented in the present paper.

B. Differential cross section

The differential cross section is calculated by

$$\frac{d\sigma}{d\Omega} = \frac{N/\varepsilon_d\varepsilon_t\varepsilon_a}{N_0 N_T \Omega}, \tag{3}$$

where

N: number of detected reaction events,
ε_d: detection efficiency for ^{12}C,
ε_t: trigger efficiency,
ε_a: efficiency of data analysis,
N_0: number of incident nuclei,
N_T: number of target nuclei per square centimeter, and
Ω: solid angle of detection.

The collected charge for the incident particles was measured by a Faraday cup connected to a current integrator. In the data analysis, the total number of pulses from the current integrator was used for each run. Using the charge state for the incident

carbon (6^+) and the measured total charge, N_0 was obtained. In the calculation of the differential cross section, the efficiencies (ε_d, ε_t, and ε_a) were determined from the data itself. The average efficiency ($\varepsilon_d\varepsilon_t\varepsilon_a$) for all runs was about 75%.

The differential cross sections for the observed states in the present experiment are extracted based on Eq. (3). Here, we considered uncertainties in the beam intensity, the target thickness, the solid angle, efficiencies, and state selections. Actually, two cross sections of a scattering angle determined by different central angular settings of the spectrometer did not necessarily agree perfectly at the overlapping angles. The differences were less than 10% in all cases. This inconsistency was due to unknown systematic errors between the data for different angular settings. The shapes of the differential cross sections agree very well, so that the relative errors in the differential cross sections are much smaller. To determine the absolute differential cross sections, the elastic-scattering differential cross sections were renormalized to the average absolute values for the 2.0°, 2.5°, 3.5°, and 5.0° data so that all the data were connected with a single differential-cross-section curve. The renormalization factor for each setting angle was consistently used for the other excited states. Systematic errors of ±10% were added for the absolute values of the cross sections. The relative errors are much smaller than the size of the marks and are shown by error bars in the figures.

The spectrum above 6 MeV includes contributions from the three states at 7.65, 9.64 and 10.30 MeV and simultaneous 4.44 MeV excitations, and thus it is extremely difficult to reliably obtain the differential cross sections for individual states separately for all angles. Therefore, we present the differential cross sections for the sum of these peaks. The contributions of the tail from higher excitations above 12 MeV and the continuum were subtracted under several shape assumptions. The uncertainty observed in the different shape assumptions was considered as an error in the cross sections. These errors were included in the individual data points.

The angular spread of the incident ^{12}C beam was measured by using a faint beam and sieve slit. The beam spread was found to be less than 0.105° FWHM. The obtained $^{12}\mathrm{C} + p$ scattering differential cross sections by a polyethylene target $(\mathrm{CH}_2)_n$ were consistent with the previous data [33] within the error bars.

The obtained differential cross sections in the center of mass frame are tabulated in Sec. VI.

IV. THEORETICAL ANALYSIS

In the following study, we investigate the effect of 3BFs on the $^{12}\mathrm{C} + {}^{12}\mathrm{C}$ elastic and inelastic cross sections. We apply three types of complex G-matrix interactions in the framework of a microscopic coupled-channel (MCC) calculation. The G-matrix interaction derived from the realistic NN interactions is the most reliable density-dependent NN interaction for analyzing the nuclear structure and reactions. The Bethe–Goldstone G-matrix equation describes two-body scattering in a nuclear medium, including the effects of Pauli blocking and the starting-energy dependence. The starting energy is the initial energy of the two nucleons in the nuclear medium. The complex G-matrix interaction is obtained by solving the G-matrix equation with the scattering boundary conditions in the nuclear medium. We apply both the real and imaginary parts of the complex G-matrix interaction to construct the complex nucleus-nucleus potentials.

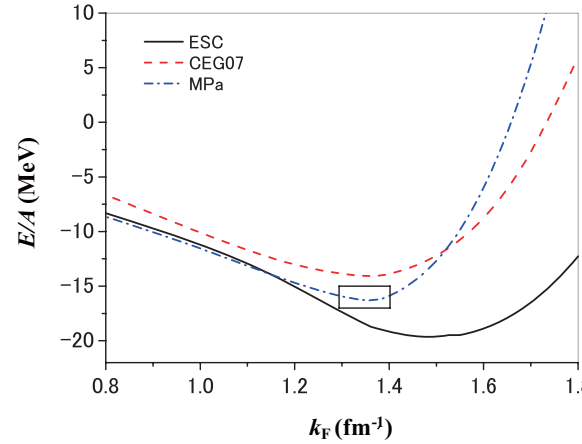

FIG. 5. Saturation curves obtained based on ESC, CEG07b, and MPa interactions. The horizontal and vertical axes represent the Fermi momentum and the binding energy per nucleon, respectively. The box shows the empirical value [36].

A. Interaction model

First, we briefly introduce the three types of complex G-matrix interactions, which are named as ESC, CEG07b, and MPa. The CEG07b [13,16] and MPa [26,27] interactions include the effect of a 3BF composed of repulsive and attractive parts.

The two-body interaction ESC denotes the ESC08 NN interaction model, which is the latest version of the meson exchange potential from the Nijmegen group [37–40]. The saturation curve for the nuclear matter obtained by ESC does not satisfy the saturation property as shown in Fig. 5. CEG07b is based on the ESC04 NN interaction model, which is the older version of ESC08 and includes a 3BF effect. The repulsive part of the 3BF is expressed by reducing the vector-meson masses as the distill increases. [38]. The attractive part of the 3BF is described by the Fujita–Miyazawa diagram [41]. Due to the 3BF effect, the saturation curve for the nuclear matter is better reproduced as shown in Fig. 5. The CEG07b interaction has often been applied to the proton-nucleus and nucleus-nucleus scatterings by three of the present authors (T.F., Y.S., and Y.Y.) [13,16–18,42,43].

MPa is based on the ESC08 NN interaction and includes a three-body repulsive part expressed by the multi-Pomeron exchange potential (MPP). Its attractive part is given phenomenologically. MPa gives the most reliable saturation properties, as seen in Fig. 5. In addition, MPa has been applied not only to the nucleus-nucleus scattering system but also to hypernuclei and neutron stars [26,27,44].

B. Theoretical frame of microscopic coupled-channel method

The collective excitation of nuclei is known to play an important role in heavy-ion reactions. The strong coupling

between the ground and low-lying collective states of colliding nuclei requires a nonperturbative treatment to properly account for the coupling effects on the elastic and inelastic scattering. The coupled-channel method is one of the most reliable and established reaction theories for studying the role of nuclear excitations in heavy-ion reactions and for extracting nuclear structure information through a coupled-channel analysis of the experimental data [45]. In the present study, the MCC method is applied to take into account such collective excitation effects on the elastic and inelastic cross sections.

In the MCC calculation, the diagonal ($\alpha = \beta$) and transition ($\alpha \neq \beta$) potentials are derived from a microscopic viewpoint. The microscopic potentials usually have the direct ($U^{(D)}$) and exchange ($U^{(EX)}$) parts,

$$U_{\alpha(ij)\to\beta(kl)} = U^{(D)}_{\alpha(ij)\to\beta(kl)} + U^{(EX)}_{\alpha(ij)\to\beta(kl)}, \tag{4}$$

where α and β represent the channel numbers and i, j, k, and l indicate the states of the projectile or target nuclei. The direct part of the potential is given by

$$U^{(D)}_{\alpha(ij)\to\beta(kl)}(\boldsymbol{R}) = \int \rho^{(P)}_{i\to k}(\boldsymbol{r_P})\rho^{(T)}_{j\to l}(\boldsymbol{r_T})v_D(\boldsymbol{s},\rho,E/A)d\boldsymbol{r_P}d\boldsymbol{r_T}, \tag{5}$$

and the exchange part by

$$U^{(EX)}_{\alpha(ij)\to\beta(kl)}(\boldsymbol{R}) = \int \rho^{(P)}_{i\to k}(\boldsymbol{r_P},\boldsymbol{r_P}-\boldsymbol{s})\rho^{(T)}_{j\to l}(\boldsymbol{r_T},\boldsymbol{r_T}+\boldsymbol{s})v_{EX} \times (\boldsymbol{s},\rho,E/A)\exp\left(\frac{i\boldsymbol{k}(\boldsymbol{R})\cdot\boldsymbol{s}}{M}\right)d\boldsymbol{r_P}d\boldsymbol{r_T}. \tag{6}$$

Here, $\boldsymbol{s} = \boldsymbol{r_P} + \boldsymbol{R} - \boldsymbol{r_T}$. The density matrix $\rho(\boldsymbol{a},\boldsymbol{b})$ is expanded by the usual density in the same manner as in Ref. [46]. The exponential function is derived from the plane-wave representation for the NN relative motion [47–49]. $\boldsymbol{k}(\boldsymbol{R})$ is the local momentum for the nucleus-nucleus relative motion. M is the reduced mass for the reaction system. The superscripts P and T for the transition density $\rho^{(P,T)}_{a\to b}$, indicate the projectile and target nuclei, respectively. ρ and E/A in the interaction $v_{D,EX}$ are the local density and the incident energy per nucleon, respectively. The detailed calculation method has been previously reported [43].

In the present calculation, the so-called frozen-density approximation is used for evaluating the local density. The local density is evaluated at the positions of each nucleon for the direct part, and at the middle point of an interacting nucleon pair for the exchange part. To construct of the transition potential, the local density is evaluated by averaging the densities of the colliding nuclei in the initial and final states. Finally, the evaluated local density is defined by

$$\rho = \frac{1}{2}\left(\rho^{(P)}_{i\to i} + \rho^{(P)}_{k\to k}\right) + \frac{1}{2}\left(\rho^{(T)}_{j\to j} + \rho^{(T)}_{l\to l}\right). \tag{7}$$

Generally, the optical potential of nucleus-nucleus systems is composed of real and imaginary parts. The imaginary part represents all the fluxes escaping from the elastic-scattering channel through all possible open reaction channels. It is difficult to completely simulate these flux losses with the imaginary part. To compensate for this, the renormalization factor N_W is introduced phenomenologically for the imaginary part of the folding model potential, which is written as

$$U = V + iN_W W. \tag{8}$$

Here, V and W are the real and imaginary parts of the double folding potential, respectively. The Coulomb potential is also obtained by folding the proton densities of the projectile and target nuclei with the NN Coulomb interaction. N_W is the only parameter used for fitting to the experimental data. Details on the method for determining the value are given in the next section.

V. RESULTS AND DISCUSSION

The experimental differential cross sections were analyzed by the MCC method with a complex optical potential. In the MCC calculation, we used the microscopic transition densities for the ^{12}C nucleus obtained by the 3α-RGM (resonance group method) [50] calculation, that reproduces the electron-scattering form factors for the ^{12}C nucleus. The states in the MCC calculation included the ground state (0^+_1), the 4.44 MeV (2^+_1) state, the 7.65 MeV (0^+_2) state, and the 9.64 MeV (3^-_1) state. In addition to those states, we included two 0^+ states and three 2^+ states that the RGM calculation predicted at higher excitation energies up to 16 MeV. It should be noted that the additional states are taken to be discretized continuum states, except for the second 2^+ state [50]. In the present MCC calculations, the single and mutual excitation of ^{12}C to the above-mentioned states is taken into account fully in the CC calculation. The calculation without the channel coupling (CC) effect is called the 1-ch calculation.

A. Single-channel calculations

First, we tested three types of complex G-matrix interactions in a single-channel (1-ch) calculation. Here, the N_W value is fixed by the reaction cross section because the cross section is very sensitive to the strength of the imaginary potential.

Figure 6 shows the calculated reaction cross section and the experimental data. The N_W values for the three types of the interactions are given in the legend of the figure. Using the N_W values determined from the reaction cross section, there is no additional free parameter when we analyze the elastic scattering. The calculated differential cross sections for 100A MeV ^{12}C + ^{12}C elastic scattering in the 1-ch calculation with the fixed N_W values are shown in Fig. 7. The solid, dashed and dot-dashed curves represent the calculation results with the ESC, CEG07b, and MPa interactions, respectively. The open circles denote the present experimental data measured in the present experiment. The ESC model based only on the two-body interaction does not reproduce the experimental differential cross sections, except for the most forward angles. On the other hand, the CEG07b and MPa models give better fits to the data. The CEG07b model reproduces the differential cross sections reasonably well for the whole angular range, while the MPa model gives a slightly worse fit than that of the CEG07b model. The calculated values for the MPa model are slightly larger than those for the CEG07b model. The two

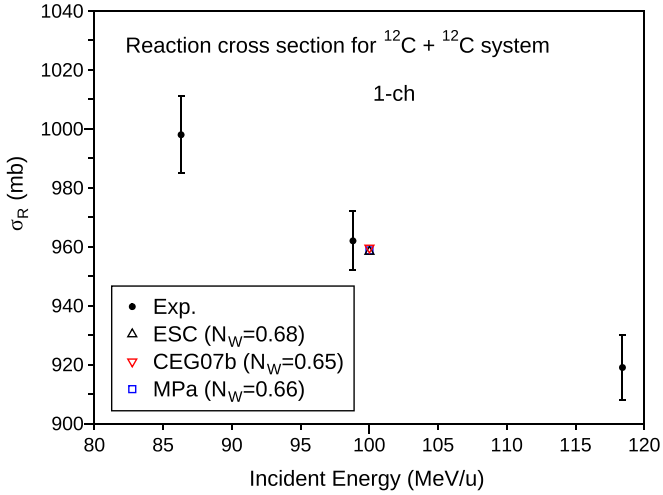

FIG. 6. Calculated $^{12}C + ^{12}C$ reaction cross sections for different complex G-matrix interactions and σ_R data as a function of beam energy. The filled circles represent the reaction cross section experimental data of Takechi [51]; the other open symbols denote 1-ch calculations for the three kinds of interaction models.

models including the 3BF effect reproduce the data better than the ESC interaction model without the 3BF effect. This result suggests an important role for the 3BF effect in nucleus-nucleus elastic scattering.

B. Full-coupled-channel calculations

The 1-ch calculation suggests that the 3BF makes an important contribution to elastic scattering. However, the coupled-channel effect needs to be included in the calculations to confirm this result. The differential cross sections were calculated using the MCC framework including the CC effect. The three interaction models are applied in the MCC

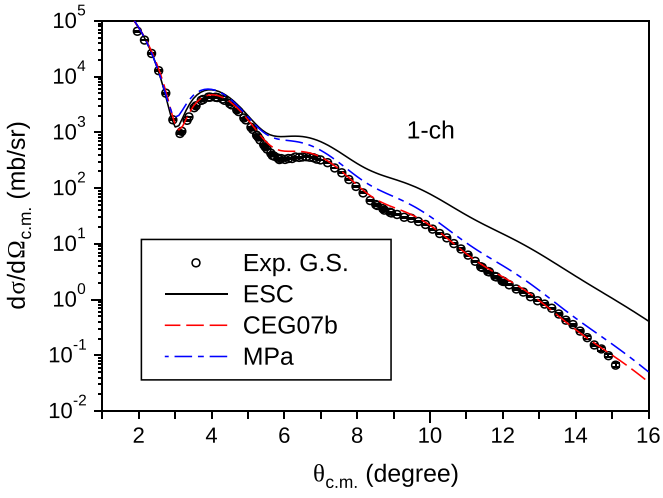

FIG. 7. 1-ch calculation results for elastic-scattering differential cross sections for $^{12}C + ^{12}C$ scattering at 100A MeV based on ESC (solid curve), CEG07b (dashed curve), and MPa (dot-dashed curve) interaction models in center-of-mass frame.

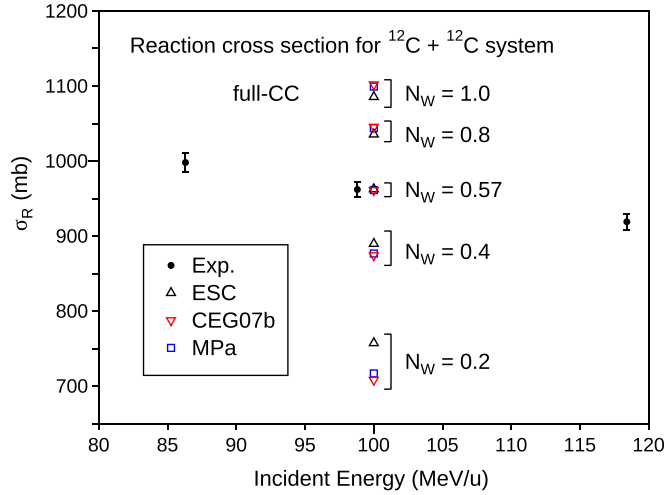

FIG. 8. Calculated reaction cross sections for the full-CC calculation with three kinds of interaction model. The results for several N_W values are also shown.

calculations. Here, we examine the suitable N_W values that reproduce the experimental data for the cross section in the MCC calculation. Figure 8 shows the sensitivity of the cross sections to the value of N_W in the CC calculation, from which we can determine the N_W values to be used in the CC calculation. We use $N_W = 0.57$ in most of the following MCC calculations. An exception is shown in Fig. 12 for studying the sensitivity of N_W value in the differential cross sections. This implies that there is no additional free parameter in the MCC calculations.

The calculated differential cross sections based on the ESC model are shown in Fig. 9. The solid and dashed curves are the calculated elastic and inelastic cross sections, respectively. The dot-dashed curve shows the result of the sum of several

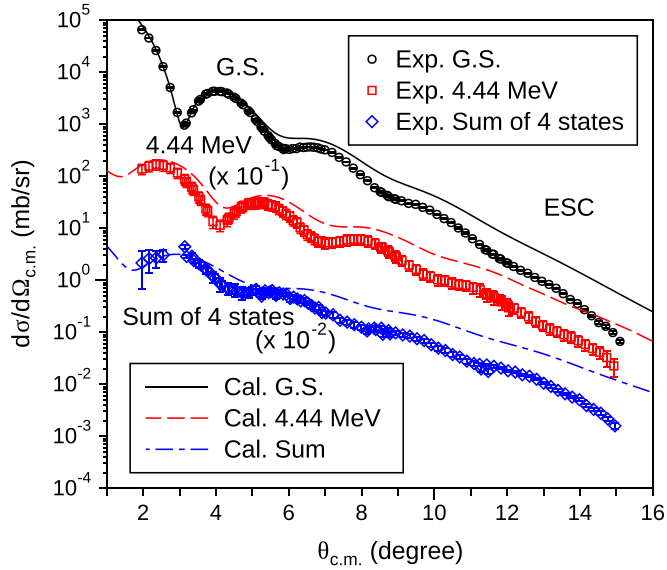

FIG. 9. Experimental and calculated differential cross sections with ESC model (without the 3BF) for $^{12}C + ^{12}C$ scattering at 100A MeV with $N_W = 0.57$ in full-CC calculation.

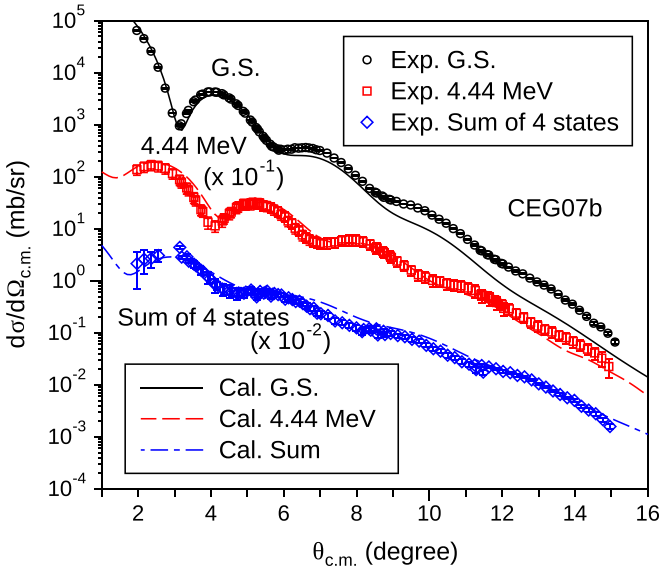

FIG. 10. Experimental and calculated differential cross sections with CEG07b model (with the 3BF) for $^{12}C + ^{12}C$ scattering at $100A$ MeV with $N_W = 0.57$ in full-CC calculation.

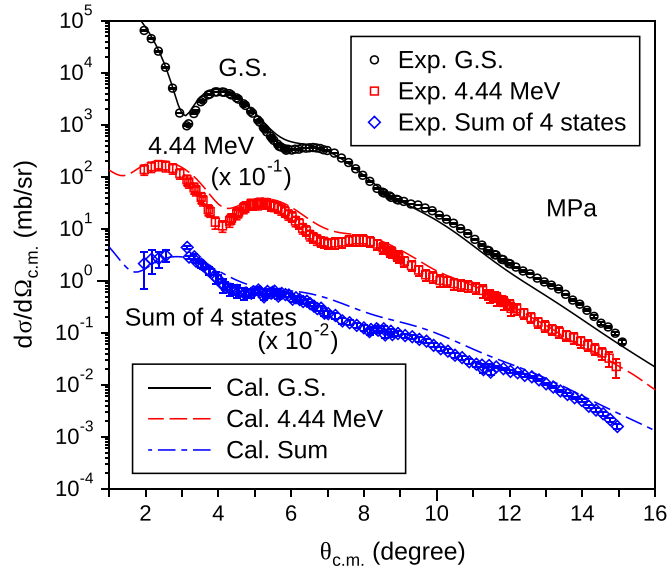

FIG. 11. Experimental and calculated differential cross sections with MPa model (with 3BF) for $^{12}C + ^{12}C$ scattering at $100A$ MeV with $N_W = 0.57$ in full-CC calculation.

inelastic cross sections, defined by

$$\sigma_{Sum} = \tfrac{1}{2}\left(\sigma_{^{12}C(0_2^+)+^{12}C(G.S.)} + \sigma_{^{12}C(3_1^-)+^{12}C(G.S.)}\right) + \sigma^{(J=0)}_{^{12}C(2_1^+)+^{12}C(2_1^+)} + \sigma^{(J=2)}_{^{12}C(2_1^+)+^{12}C(2_1^+)} + \sigma^{(J=4)}_{^{12}C(2_1^+)+^{12}C(2_1^+)}. \quad (9)$$

The factor $\frac{1}{2}$ is included for the single-excitation cross sections to the 0_2^+ and 3_1^- unbound excited states located above the 3α threshold, because the calculated cross sections for these inelastic channels include events in which either the projectile ^{12}C or the target ^{12}C is excited to the unbound states, while the experimental data do not include the projectile-excited events, as mentioned above. The 2_2^+ excited state has not yet been firmly established [52] and, therefore, we do not include the 2_2^+ excited state in the sum of inelastic cross sections in the theoretical calculations. In addition, we note that the calculation results are slightly different to those in Ref. [21]. Consequently, the factor $\frac{1}{2}$ is added for the mutual excited states in Ref. [21]. The calculated sum of several inelastic cross sections is then slightly larger than that in Ref. [21].

Even if the CC effect is included, ESC does not accurately reproduce the elastic or inelastic scatterings, particularly at backward angles, as shown in Fig. 9.

In Figure 10, we compare the results of the full-CC calculation with the CEG07b model with experimental values. The elastic cross sections are well reproduced at small scattering angles. However, the calculated elastic cross sections slightly underestimate the experimental values for angles larger than 6.0°. The CEG07b interaction slightly overestimates the saturation energy for EOS and is softer than the MPa interaction, as shown in Fig. 5. This softness may decrease the elastic cross sections for backward angles. In addition, the strong coupling effect from the 2_1^+ state causes a decrease in the cross section. Details of the CC effect are described in the next section. For the inelastic cross section of a single excitation of the 2_1^+ state, the calculated and experimental values are in good agreement.

Although the CEG07b model, which includes three-body repulsion, reproduces the experimental data better than the ESC model, it fails to reproduce the elastic cross section over the entire angular range, and particularly at the large angles. Here, we tested and confirmed that a small change in N_W has a negligible effect on the elastic cross section.

The full-CC calculation results with the MPa model are shown in Fig. 11. The elastic and inelastic cross sections are reproduced for the whole range of scattering angles except for a slight overestimation of the cross section for the sum of the four states (the dot-dashed curve). The MPa interaction model provides the best overall description of the experimental data for both the elastic and inelastic cross sections. It is considered that a change in EOS between the CEG07b and MPa interactions, as shown in Fig. 5, emerges for the elastic cross section. The MPa interaction reproduces well the elastic and inelastic cross sections. We described below a detailed analysis based on the MPa interaction.

Here we show the effect of the renormalization factor N_W on the elastic and inelastic cross sections in the full-CC calculation with the MPa interaction. The calculated elastic and inelastic cross sections are shown in Fig. 12. The dotted, short-dashed, solid, dot-dashed, and dot-dot-dashed curves show the calculated elastic cross sections with $N_W = 0.2$, 0.4, 0.57, 0.8, and 1.0, respectively. The bold (red) dotted, short-dashed, dashed, dot-dashed, and dot-dot-dashed curves are the results of the inelastic cross section calculated with $N_W = 0.2$, 0.4, 0.57, 0.8, and 1.0, respectively. The effect of the N_W value is clearly seen in the elastic and inelastic cross sections. The same trend for N_W was also seen in Ref. [16] for the $^{16}O + ^{16}O$ system in the 1-ch calculation with the CEG07a interaction (without the 3BF). We note that the N_W value is multiplied not only by the diagonal potentials but also by

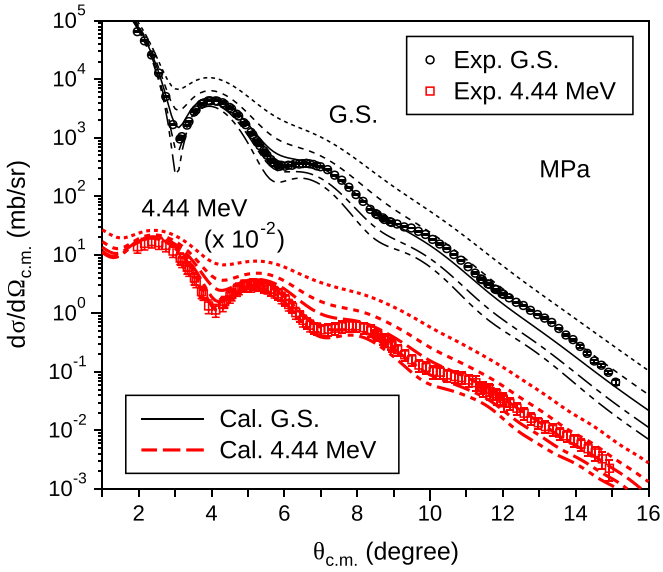

FIG. 12. Experimental and calculated differential cross sections with MPa model (with the 3BF) for $^{12}C + ^{12}C$ scattering at $100A$ MeV with several N_W values in full-CC calculation. The meaning of the curves is described in the text.

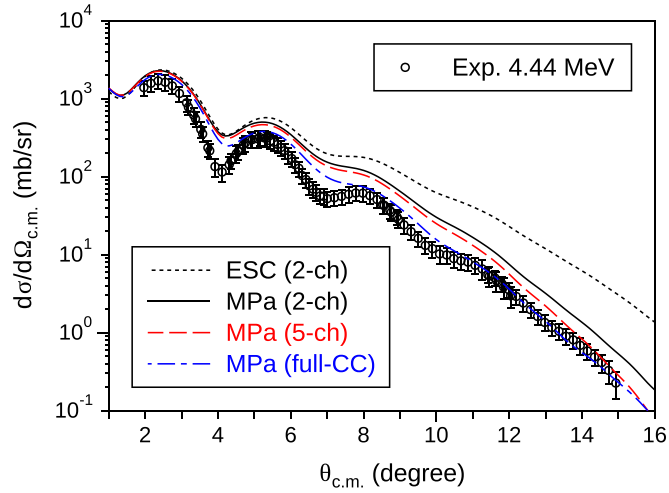

FIG. 14. Inelastic cross section for 4.44 MeV. The dotted and solid curves are the 2-ch (elastic and singe excited channels) results with ESC and MPa interactions, respectively. The dashed and dot-dashed curves are the 5-ch [elastic, singe 2_1^+ excited, mutual 2_1^+ excited ($J = 0,2,4$) channels] and full-CC results with the MPa interaction, respectively.

the transition potentials in our MCC calculation. Therefore, the effect of N_W effect on the elastic cross section cannot be readily understood in the MCC calculation. In addition, the effect of the N_W value on the inelastic cross sections is more complicated to understand.

C. Details of coupled-channel effect on elastic and inelastic cross sections

Details of the CC effect with the MPa interaction are presented in Fig. 13. As described above, we use $N_W = 0.57$.

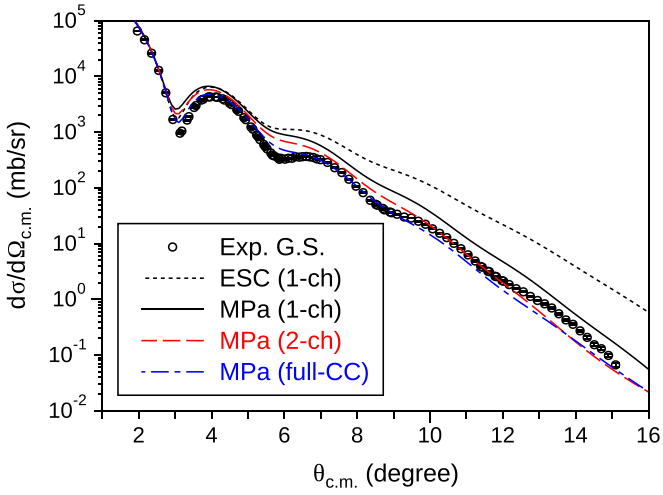

FIG. 13. Elastic cross section for $^{12}C + ^{12}C$ at $E/A = 100$ MeV. The dotted and solid curves are the results with the ESC and MPa interactions, respectively. The dashed and dot-dashed curves are the results of the 2-ch (elastic and singe 2_1^+ excited channels) and full-CC calculations with MPa, respectively.

The CC effect for the MPa interaction is seen in the elastic differential cross sections as a decrease of the cross section at large scattering angles. The dashed curve is obtained by a 2-ch calculation, which includes the ground and excited (2_1^+) states. The effect of coupling on the higher excited states is smaller, as shown by the dot-dashed line. The change in the cross section is largest from ESC to MPa and is much larger than the changes due to the CC effect. Therefore, the 3BF effect is the most important factor for reproducing the elastic cross section.

Figure 14 presents the results of the 2-ch calculation, including the ground and the 2_1^+ excited states, the 5-ch calculation, including the ground state, 2_1^+ excitation and the mutual 2_1^+ excitation ($J = 0,2,4$), and the full-CC calculation. The inelastic scattering is better reproduced with the inclusion of the CC effect. However, here also the 3BF effect is larger than the CC effect. The effects of the excitations on higher excited states, such as the 0_2^+, 2_2^+, and 2_3^+ states, were also estimated. The effects of those states was found to be negligibly small and thus are not shown in the figure. For the inelastic cross section, the 3BF effect is also clearly seen to be important. However, including only the 3BF effect does not satisfactorily reproduce the data. The calculated result reproduces well the data up to backward angles only when the CC effects are included. The mutual 2_1^+ excited ($J = 0,2,4$) channels substantially contribute to the inelastic cross section as shown in Fig. 14. However, the 0_2^+, 2_2^+ and 2_3^+ states contribute very weakly and the effects are not shown in the figure. Here, we note that the calculated result of the ESC (2-ch) does not reproduce the elastic cross section. However, the 3BF effect on the inelastic cross section is not revealed in this stage. A detailed analysis for the 3BF effect on the inelastic cross section is performed with the elastic cross section in the next section.

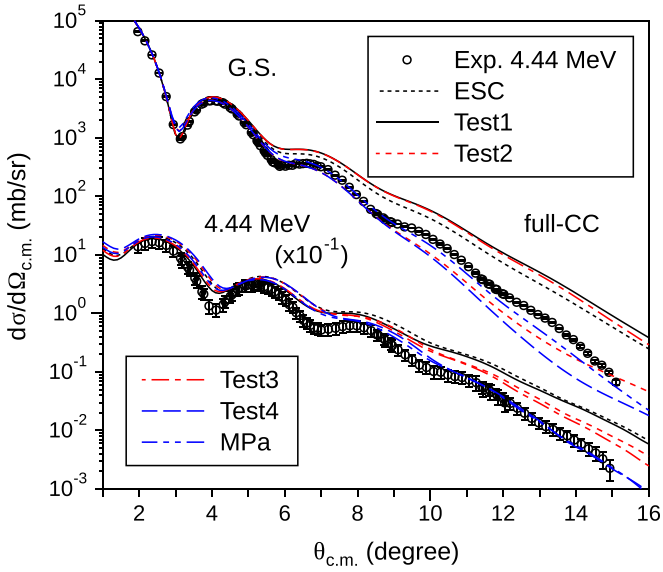

FIG. 15. Elastic and inelastic cross sections for $^{12}C + ^{12}C$ at $E/A = 100$ MeV. The dotted and dot-dot-dashed curves are the results with the ESC and MPa interactions, respectively. The meanings of the curves are described in the text.

D. Role of 3BF effect on diagonal and transition potentials

Finally, we investigate the 3BF effect on the elastic and inelastic cross sections in detail, as shown in Fig. 15. To identify the crucial potential in the MCC calculation with the 3BF effect on the inelastic cross section, we switch on and off on the diagonal ($\alpha = \beta$) or transition ($\alpha \neq \beta$) potentials derived from the ESC and MPa interactions. We perform four types of the tests of the potentials, as follows:

(Test 1) The solid curves in Fig. 15 are based on the MPa interaction. However, the 3BF effect on the diagonal potentials for the elastic [^{12}C(g.s.)+^{12}C(g.s.)] and single excited [^{12}C(2^+_1) +^{12}C(g.s.)] channels is switched off.

(Test 2) The short dashed curves are based on the ESC interaction. The 3BF effect on the diagonal potential for the elastic channel is switched on.

(Test 3) The dot-dashed curves are based on the MPa interaction. The 3BF effect on the diagonal potential for the elastic channel is switched off.

(Test 4) The dashed curves are based on the MPa interaction. However, the 3BF effect on all the transition potentials is switched off.

By comparing the results for MPa (dot-dot-dashed) and Test 4 (dashed), the 3BF effect on the transition potential can be seen for the elastic and inelastic cross sections. Test 4 shows that the 3BF effect plays an unimportant role in the transition potential for the inelastic cross section. On the other hand, the 3BF effect on the transition potentials appears slight in the elastic cross section for the backward angles by the CC effect. It can be clearly seen that the diagonal potential for the elastic channel plays an important role in correcting the elastic and inelastic cross sections based on the results of Test 2 (short dashed) and Test 3 (dot-dashed). The calculated elastic cross sections for Test 2 and Test 3 agree with those for MPa and ESC, respectively. Namely, the 3BF effect on the elastic channel potential almost corrects the elastic cross section. The calculated inelastic cross sections for Test 2 and Test 3 are located halfway between the results for MPa and ESC. This implies that the 3BF effect of the diagonal potential for the elastic channel also affects the inelastic cross section. By comparing the results for MPa, Test 3, Test 1 (solid), and ESC, the important role of the 3BF of the diagonal potentials for the single excited (2^+_1) channel is clear for the inelastic cross section. The MPa result well reproduces the data up to backward angles. The calculated inelastic cross section overshoots the data when the 3BF effect on the diagonal potential for the elastic channel is switched off (Test 3). Furthermore, the calculated inelastic cross section is consistent with the ESC result when the 3BF effect on both the diagonal potentials is switched off (Test 1). The important role of the 3BF effect on the diagonal potentials for the entrance and exit channels is clearly seen in the inelastic cross section. Consequently, the 3BF effect for the diagonal potentials is the most important factor for reproducing both the elastic and the inelastic cross sections. This conclusion is consistent with the well-known sense of the distorted wave Born approximation [53].

VI. SUMMARY

In summary, the elastic and inelastic differential cross sections for $^{12}C + ^{12}C$ scattering at an incident energy of $100A$ MeV were determined by using the ring cyclotron of the Research Center for Nuclear Physics, Osaka University. The differential cross sections for the ground state (0^+_1), 4.44 MeV (2^+_1) state, and the sum of the 7.65 MeV (0^+_2) state, the 9.64 MeV (3^-_1) state and the simultaneous excitation to 4.44 MeV, were precisely obtained. The experimental data were investigated by using three different G-matrix interaction models: the ESC model based on the two-body force only, the CEG07b model with the addition of an induced three-body force, and the MPa model with three-body repulsion modeled by multi-Pomeron-exchange potential (MPP). The imaginary part of the folding potential was multiplied by a renormalization factor N_W for all interaction models to reproduce the experimental reaction cross sections. In addition, microscopic coupled-channel (MCC) calculations are performed for all three interaction models. The ESC model, which does not include the 3BF effect, failed to reproduce the measured cross sections for both the elastic and inelastic scattering. The calculations including the 3BF effect reproduced the experimental cross section better than the single-channel calculation. Among the two different models including the 3BF, the MPa model reproduced the data better than the CEG07b model. A detailed analysis of the 3BF effect on the coupled-channel potentials showed that the 3BF effect on the elastic channel potential was the most important factor for modeling the experimental data. The MPa model also demonstrated the importance of measuring the excited state in addition to the elastic scattering. The present results provide clear evidence of the important roles of the repulsive 3BF

and the CC effect in high-energy heavy-ion collisions. Further experiments at higher energies are expected to provide less model-dependent information on the repulsive nature of the 3BF.

ACKNOWLEDGMENTS

We are grateful to the RCNP Ring Cyclotron staff for providing stable carbon beams for the experiment. This work was supported by the National Nature Science Foundation of China under Grants No. 11475013, No. 11035007, and No. 11175011. The experiment was supported in part by a grant-in-aid program of the Japanese government under contract number 23224008, and in part by the RCNP-BUAA collaboration program. Part of this work was also supported by the China Postdoctoral Science Foundation (2016M591911), Natural Science Foundation of Jiangsu Province (BK20160306), National Key Scientific Instrument and Equipment Development Projects (Grant No. 2013YQ04086102), and a Project Funded by the Priority Academic Program Development of Jiangsu Higher Education Institutions(PAPD). The theoretical analysis was supported by JSPS KAKENHI Grants No. JP15H00842, No. JP15K17661, and NO. JP15K05087.

SUPPLEMENTARY INFORMATION

TABLE I. Differential cross sections for $^{12}C + ^{12}C$ scattering at an incident energy of 100*A* MeV. These cross sections include transitions to the ground state (0^+_1) and to the first-excited 4.44 MeV state (2^+_1) and the sum of the 7.65 MeV (0^+_2) state, the 9.64 MeV (3^-_1) state, the 10.30 MeV state and the simultaneous (projectile and target) excitations of the 4.44 MeV (2^+_1) state.

Angle (degree) c.m.	Cross section (mb/sr) Ground state[a]	Angle (degree) c.m.	Cross section (mb/sr) 4.44 MeV[b]	Angle (degree) c.m.	Cross section (mb/sr) Sum of 4 states
1.96	$(7.15 \pm 0.12) \times 10^4$	1.96	$(1.51 \pm 0.32) \times 10^3$	1.97	$(2.35 \pm 1.60) \times 10^2$
2.16	$(4.94 \pm 0.08) \times 10^4$	2.16	$(1.70 \pm 0.36) \times 10^3$	2.16	$(2.84 \pm 1.35) \times 10^2$
2.35	$(2.86 \pm 0.05) \times 10^4$	2.35	$(1.84 \pm 0.38) \times 10^3$	2.36	$(2.95 \pm 1.05) \times 10^2$
2.55	$(1.40 \pm 0.02) \times 10^4$	2.55	$(1.76 \pm 0.38) \times 10^3$	2.55	$(3.35 \pm 0.86) \times 10^2$
2.74	$(5.55 \pm 0.10) \times 10^3$	2.75	$(1.59 \pm 0.33) \times 10^3$	3.14	$(4.80 \pm 0.42) \times 10^2$
2.94	$(1.85 \pm 0.04) \times 10^3$	2.94	$(1.27 \pm 0.26) \times 10^3$	3.34	$(3.18 \pm 0.41) \times 10^2$
3.13	$(1.04 \pm 0.02) \times 10^3$	3.14	$(9.59 \pm 2.00) \times 10^2$	3.53	$(2.29 \pm 0.39) \times 10^2$
3.33	$(1.80 \pm 0.04) \times 10^3$	3.33	$(6.73 \pm 1.50) \times 10^2$	3.73	$(1.73 \pm 0.29) \times 10^2$
3.52	$(3.04 \pm 0.06) \times 10^3$	3.53	$(4.40 \pm 0.97) \times 10^2$	3.92	$(1.28 \pm 0.32) \times 10^2$
3.72	$(4.10 \pm 0.08) \times 10^3$	3.72	$(2.55 \pm 0.57) \times 10^2$	4.12	$(9.19 \pm 2.72) \times 10^1$
3.91	$(4.69 \pm 0.09) \times 10^3$	3.92	$(1.47 \pm 0.36) \times 10^2$	4.32	$(7.64 \pm 2.04) \times 10^1$
4.11	$(4.68 \pm 0.09) \times 10^3$	4.11	$(1.25 \pm 0.29) \times 10^2$	4.51	$(7.17 \pm 1.99) \times 10^1$
4.30	$(4.35 \pm 0.08) \times 10^3$	4.31	$(1.55 \pm 0.36) \times 10^2$	4.71	$(6.29 \pm 1.66) \times 10^1$
4.50	$(3.59 \pm 0.07) \times 10^3$	4.50	$(2.14 \pm 0.49) \times 10^2$	4.90	$(6.33 \pm 1.28) \times 10^1$
4.69	$(2.78 \pm 0.05) \times 10^3$	4.70	$(2.80 \pm 0.62) \times 10^2$	5.10	$(7.32 \pm 1.18) \times 10^1$
4.89	$(1.99 \pm 0.04) \times 10^3$	4.89	$(3.29 \pm 0.72) \times 10^2$	5.29	$(6.21 \pm 1.09) \times 10^1$
5.08	$(1.36 \pm 0.03) \times 10^3$	5.09	$(3.34 \pm 0.76) \times 10^2$	5.49	$(6.60 \pm 0.99) \times 10^1$
5.28	$(9.06 \pm 0.21) \times 10^2$	5.29	$(3.41 \pm 0.75) \times 10^2$	5.69	$(6.06 \pm 0.97) \times 10^1$
5.47	$(6.05 \pm 0.16) \times 10^2$	3.19	$(8.44 \pm 1.69) \times 10^2$	3.19	$(3.12 \pm 0.22) \times 10^2$
5.67	$(4.25 \pm 0.13) \times 10^2$	3.38	$(6.01 \pm 1.20) \times 10^2$	3.39	$(2.61 \pm 0.24) \times 10^2$
5.86	$(3.56 \pm 0.11) \times 10^2$	3.58	$(3.85 \pm 0.79) \times 10^2$	3.58	$(2.15 \pm 0.28) \times 10^2$
3.18	$(1.14 \pm 0.01) \times 10^3$	3.77	$(2.33 \pm 0.48) \times 10^2$	3.78	$(1.65 \pm 0.22) \times 10^2$
3.38	$(2.08 \pm 0.02) \times 10^3$	4.36	$(1.74 \pm 0.36) \times 10^2$	3.98	$(1.21 \pm 0.20) \times 10^2$
3.57	$(3.29 \pm 0.03) \times 10^3$	4.56	$(2.29 \pm 0.48) \times 10^2$	4.17	$(9.01 \pm 1.63) \times 10^1$
3.77	$(4.25 \pm 0.04) \times 10^3$	4.75	$(2.95 \pm 0.63) \times 10^2$	4.37	$(7.46 \pm 1.49) \times 10^1$
3.96	$(4.70 \pm 0.05) \times 10^3$	4.95	$(3.26 \pm 0.67) \times 10^2$	4.56	$(6.81 \pm 1.27) \times 10^1$
4.16	$(4.63 \pm 0.05) \times 10^3$	5.14	$(3.48 \pm 0.72) \times 10^2$	4.76	$(6.42 \pm 1.02) \times 10^1$
4.35	$(4.13 \pm 0.04) \times 10^3$	5.34	$(3.39 \pm 0.70) \times 10^2$	4.95	$(6.67 \pm 0.92) \times 10^1$
4.55	$(3.40 \pm 0.03) \times 10^3$	5.53	$(3.01 \pm 0.62) \times 10^2$	5.15	$(6.70 \pm 0.81) \times 10^1$
4.74	$(2.59 \pm 0.03) \times 10^3$	5.73	$(2.57 \pm 0.53) \times 10^2$	5.35	$(6.87 \pm 0.66) \times 10^1$
4.94	$(1.84 \pm 0.02) \times 10^3$	5.92	$(2.06 \pm 0.43) \times 10^2$	5.54	$(6.95 \pm 0.66) \times 10^1$
5.13	$(1.24 \pm 0.01) \times 10^3$	6.12	$(1.55 \pm 0.32) \times 10^2$	5.74	$(6.28 \pm 0.52) \times 10^1$
5.33	$(8.04 \pm 0.09) \times 10^2$	6.31	$(1.13 \pm 0.24) \times 10^2$	5.93	$(5.87 \pm 0.48) \times 10^1$
5.52	$(5.50 \pm 0.07) \times 10^2$	6.51	$(8.32 \pm 1.79) \times 10^1$	6.13	$(5.18 \pm 0.47) \times 10^1$
5.72	$(4.10 \pm 0.05) \times 10^2$	6.70	$(6.85 \pm 1.48) \times 10^1$	6.32	$(4.39 \pm 0.41) \times 10^1$
5.91	$(3.72 \pm 0.05) \times 10^2$	6.90	$(6.10 \pm 1.27) \times 10^1$	6.52	$(4.00 \pm 0.37) \times 10^1$

TABLE I. *(Continued.)*

Angle (degree) c.m.	Cross section (mb/sr) Ground state[a]	Angle (degree) c.m.	Cross section (mb/sr) 4.44 MeV[b]	Angle (degree) c.m.	Cross section (mb/sr) Sum of 4 states
6.11	$(3.73 \pm 0.05) \times 10^{2}$	5.44	$(3.14 \pm 0.64) \times 10^{2}$	6.72	$(3.21 \pm 0.37) \times 10^{1}$
6.30	$(3.97 \pm 0.05) \times 10^{2}$	5.63	$(2.82 \pm 0.58) \times 10^{2}$	6.91	$(2.62 \pm 0.31) \times 10^{1}$
6.50	$(3.97 \pm 0.05) \times 10^{2}$	5.83	$(2.35 \pm 0.48) \times 10^{2}$	5.25	$(5.39 \pm 0.71) \times 10^{1}$
6.69	$(3.94 \pm 0.05) \times 10^{2}$	6.03	$(1.86 \pm 0.38) \times 10^{2}$	5.45	$(6.35 \pm 0.68) \times 10^{1}$
6.89	$(3.63 \pm 0.05) \times 10^{2}$	6.22	$(1.40 \pm 0.29) \times 10^{2}$	5.64	$(5.59 \pm 0.72) \times 10^{1}$
5.23	$(9.75 \pm 0.14) \times 10^{2}$	6.42	$(1.00 \pm 2.07) \times 10^{2}$	5.84	$(5.96 \pm 0.58) \times 10^{1}$
5.43	$(6.61 \pm 0.10) \times 10^{2}$	6.61	$(7.55 \pm 1.57) \times 10^{1}$	6.04	$(4.86 \pm 0.62) \times 10^{1}$
5.62	$(4.65 \pm 0.07) \times 10^{2}$	6.81	$(6.17 \pm 1.28) \times 10^{1}$	6.23	$(4.79 \pm 0.53) \times 10^{1}$
5.82	$(3.79 \pm 0.06) \times 10^{2}$	7.00	$(5.70 \pm 1.18) \times 10^{1}$	6.43	$(4.45 \pm 0.49) \times 10^{1}$
6.01	$(3.59 \pm 0.06) \times 10^{2}$	7.20	$(5.86 \pm 1.20) \times 10^{1}$	6.62	$(3.58 \pm 0.45) \times 10^{1}$
6.21	$(3.72 \pm 0.06) \times 10^{2}$	7.39	$(6.13 \pm 1.27) \times 10^{1}$	6.82	$(3.28 \pm 0.37) \times 10^{1}$
6.40	$(3.90 \pm 0.06) \times 10^{2}$	7.59	$(6.49 \pm 1.38) \times 10^{1}$	7.01	$(2.56 \pm 0.30) \times 10^{1}$
6.60	$(4.02 \pm 0.06) \times 10^{2}$	7.78	$(6.72 \pm 1.38) \times 10^{1}$	7.21	$(2.37 \pm 0.30) \times 10^{1}$
6.79	$(3.85 \pm 0.06) \times 10^{2}$	7.98	$(6.73 \pm 1.39) \times 10^{1}$	7.41	$(1.87 \pm 0.24) \times 10^{1}$
6.99	$(3.51 \pm 0.06) \times 10^{2}$	8.17	$(6.22 \pm 1.29) \times 10^{1}$	7.60	$(1.72 \pm 0.20) \times 10^{1}$
7.18	$(3.13 \pm 0.05) \times 10^{2}$	8.37	$(5.59 \pm 1.18) \times 10^{1}$	7.80	$(1.53 \pm 0.18) \times 10^{1}$
7.38	$(2.53 \pm 0.04) \times 10^{2}$	8.56	$(4.68 \pm 0.99) \times 10^{1}$	7.99	$(1.38 \pm 0.17) \times 10^{1}$
7.57	$(2.07 \pm 0.03) \times 10^{2}$	8.76	$(3.84 \pm 0.81) \times 10^{1}$	8.19	$(1.27 \pm 0.17) \times 10^{0}$
7.77	$(1.57 \pm 0.03) \times 10^{2}$	8.96	$(3.09 \pm 0.67) \times 10^{1}$	8.38	$(1.24 \pm 0.13) \times 10^{1}$
7.96	$(1.18 \pm 0.02) \times 10^{2}$	8.52	$(4.76 \pm 0.99) \times 10^{1}$	8.58	$(9.99 \pm 1.24) \times 10^{0}$
8.16	$(8.98 \pm 0.17) \times 10^{1}$	8.72	$(4.04 \pm 0.83) \times 10^{1}$	8.78	$(1.02 \pm 0.12) \times 10^{1}$
8.35	$(6.60 \pm 0.13) \times 10^{1}$	8.91	$(3.36 \pm 0.69) \times 10^{1}$	8.15	$(1.17 \pm 0.15) \times 10^{1}$
8.55	$(5.35 \pm 0.11) \times 10^{1}$	9.11	$(2.62 \pm 0.55) \times 10^{1}$	8.34	$(1.32 \pm 0.16) \times 10^{1}$
8.74	$(4.44 \pm 0.10) \times 10^{1}$	9.31	$(2.16 \pm 0.45) \times 10^{1}$	8.54	$(1.32 \pm 0.14) \times 10^{1}$
8.94	$(3.93 \pm 0.09) \times 10^{1}$	9.50	$(1.77 \pm 0.37) \times 10^{1}$	8.73	$(1.18 \pm 0.12) \times 10^{1}$
8.51	$(5.59 \pm 0.09) \times 10^{1}$	9.70	$(1.44 \pm 0.31) \times 10^{1}$	8.93	$(1.07 \pm 0.11) \times 10^{1}$
8.70	$(4.69 \pm 0.08) \times 10^{1}$	9.89	$(1.31 \pm 0.28) \times 10^{1}$	9.13	$(9.73 \pm 0.91) \times 10^{0}$
8.90	$(4.07 \pm 0.07) \times 10^{1}$	10.09	$(1.12 \pm 0.26) \times 10^{1}$	9.32	$(9.28 \pm 0.91) \times 10^{0}$
9.09	$(3.69 \pm 0.07) \times 10^{1}$	10.28	$(1.09 \pm 0.23) \times 10^{1}$	9.52	$(8.23 \pm 0.76) \times 10^{0}$
9.29	$(3.31 \pm 0.06) \times 10^{1}$	10.48	$(9.76 \pm 2.07) \times 10^{0}$	9.71	$(7.64 \pm 0.68) \times 10^{0}$
9.48	$(3.15 \pm 0.06) \times 10^{1}$	10.67	$(9.14 \pm 1.92) \times 10^{0}$	9.91	$(6.34 \pm 0.57) \times 10^{0}$
9.68	$(2.78 \pm 0.05) \times 10^{1}$	10.87	$(8.80 \pm 1.86) \times 10^{0}$	10.10	$(5.46 \pm 0.56) \times 10^{0}$
9.87	$(2.46 \pm 0.05) \times 10^{1}$	11.06	$(8.01 \pm 1.76) \times 10^{0}$	10.30	$(4.91 \pm 0.47) \times 10^{0}$
10.07	$(2.03 \pm 0.04) \times 10^{1}$	11.26	$(7.20 \pm 1.88) \times 10^{0}$	10.49	$(4.11 \pm 0.41) \times 10^{0}$
10.26	$(1.69 \pm 0.04) \times 10^{1}$	11.45	$(5.84 \pm 1.56) \times 10^{0}$	10.69	$(3.69 \pm 0.36) \times 10^{0}$
10.46	$(1.41 \pm 0.03) \times 10^{1}$	11.65	$(5.10 \pm 1.36) \times 10^{0}$	10.89	$(3.06 \pm 0.33) \times 10^{0}$
10.65	$(1.11 \pm 0.03) \times 10^{1}$	11.84	$(4.21 \pm 1.11) \times 10^{0}$	11.08	$(2.76 \pm 0.30) \times 10^{0}$
10.85	$(8.92 \pm 0.23) \times 10^{0}$	12.04	$(3.26 \pm 0.89) \times 10^{0}$	11.28	$(2.17 \pm 0.27) \times 10^{0}$
11.04	$(6.92 \pm 0.19) \times 10^{0}$	11.41	$(6.05 \pm 1.26) \times 10^{0}$	11.47	$(1.94 \pm 0.21) \times 10^{0}$
11.24	$(5.37 \pm 0.17) \times 10^{0}$	11.61	$(5.51 \pm 1.10) \times 10^{0}$	11.24	$(2.65 \pm 0.19) \times 10^{0}$
11.43	$(4.16 \pm 0.14) \times 10^{0}$	11.80	$(4.67 \pm 0.97) \times 10^{0}$	11.43	$(2.60 \pm 0.14) \times 10^{0}$
11.63	$(3.48 \pm 0.13) \times 10^{0}$	12.00	$(3.86 \pm 0.80) \times 10^{0}$	11.63	$(2.44 \pm 0.13) \times 10^{0}$
11.82	$(2.81 \pm 0.11) \times 10^{0}$	12.19	$(3.19 \pm 0.68) \times 10^{0}$	11.82	$(2.27 \pm 0.11) \times 10^{0}$
12.02	$(2.33 \pm 0.10) \times 10^{0}$	12.39	$(2.65 \pm 0.57) \times 10^{0}$	12.02	$(2.00 \pm 0.11) \times 10^{0}$
11.39	$(4.28 \pm 0.08) \times 10^{0}$	12.58	$(2.17 \pm 0.46) \times 10^{0}$	12.21	$(1.89 \pm 0.09) \times 10^{0}$
11.59	$(3.52 \pm 0.07) \times 10^{0}$	12.78	$(1.78 \pm 0.38) \times 10^{0}$	12.41	$(1.69 \pm 0.09) \times 10^{0}$
11.78	$(2.89 \pm 0.06) \times 10^{0}$	12.97	$(1.49 \pm 0.32) \times 10^{0}$	12.61	$(1.57 \pm 0.08) \times 10^{0}$
11.98	$(2.39 \pm 0.05) \times 10^{0}$	13.17	$(1.28 \pm 0.28 \times 10^{0}$	12.80	$(1.38 \pm 0.07) \times 10^{0}$
12.17	$(2.03 \pm 0.05) \times 10^{0}$	13.36	$(1.14 \pm 0.25) \times 10^{0}$	13.00	$(1.16 \pm 0.06) \times 10^{0}$
12.37	$(1.72 \pm 0.04) \times 10^{0}$	13.56	$(9.92 \pm 2.18) \times 10^{-1}$	13.19	$(1.01 \pm 0.06) \times 10^{0}$
12.56	$(1.50 \pm 0.04) \times 10^{0}$	13.76	$(8.94 \pm 1.85) \times 10^{-1}$	13.39	$(8.43 \pm 0.50) \times 10^{-1}$
12.76	$(1.25 \pm 0.03) \times 10^{0}$	13.95	$(7.60 \pm 1.66) \times 10^{-1}$	13.58	$(7.26 \pm 0.43) \times 10^{-1}$
12.95	$(1.06 \pm 0.27) \times 10^{0}$	14.15	$(6.43 \pm 1.37) \times 10^{-1}$	13.78	$(6.27 \pm 0.36) \times 10^{-1}$
13.15	$(9.19 \pm 0.24) \times 10^{-1}$	14.34	$(5.41 \pm 1.17) \times 10^{-1}$	13.97	$(5.60 \pm 0.32) \times 10^{-1}$
13.34	$(7.71 \pm 0.21) \times 10^{-1}$	14.54	$(4.56 \pm 1.11) \times 10^{-1}$	14.17	$(4.29 \pm 0.29) \times 10^{-1}$

TABLE I. *(Continued.)*

Angle (degree) c.m.	Cross section (mb/sr) Ground state[a]	Angle (degree) c.m.	Cross section (mb/sr) 4.44 MeV[b]	Angle (degree) c.m.	Cross section (mb/sr) Sum of 4 states
13.54	$(6.11 \pm 0.18) \times 10^{-1}$	14.73	$(3.62 \pm 1.07) \times 10^{-1}$	14.37	$(3.66 \pm 0.27) \times 10^{-1}$
13.73	$(4.73 \pm 0.16) \times 10^{-1}$	14.93	$(2.51 \pm 0.91) \times 10^{-1}$	14.56	$(3.09 \pm 0.24) \times 10^{-1}$
13.93	$(3.95 \pm 0.14) \times 10^{-1}$			14.76	$(2.38 \pm 0.24) \times 10^{-1}$
14.12	$(3.02 \pm 0.12) \times 10^{-1}$			14.95	$(1.77 \pm 0.22) \times 10^{-1}$
14.32	$(2.31 \pm 0.10) \times 10^{-1}$				
14.51	$(1.70 \pm 0.09) \times 10^{-1}$				
14.71	$(1.44 \pm 0.08) \times 10^{-1}$				
14.90	$(1.10 \pm 0.08) \times 10^{-1}$				
15.10	$(7.38 \pm 0.58) \times 10^{-2}$				

[a]10% error has to be added in common scale of the cross section. This error comes from inconsistencies of the cross sections obtained from the different spectrometer settings.

[b]20% errors has to be added in common scale of the cross section due to the uncertainty of the estimation of simultaneous excitations of the projectile and the target to 4.44 MeV state.

[1] S. C. Pieper and R. B. Wiringa, Annu. Rev. Nucl. Part. Sci. **51**, 53 (2001).

[2] P. Navrátil and W. E. Ormand, Phys. Rev. C **68**, 034305 (2003).

[3] P. Navrátil, V. G. Gueorguiev, J. P. Vary, W. E. Ormand, and A. Nogga, Phys. Rev. Lett. **99**, 042501 (2007).

[4] T. Otsuka, T. Suzuki, J. D. Holt, A. Schwenk, and Y. Akaishi, Phys. Rev. Lett. **105**, 032501 (2010).

[5] A. Deltuva and A. C. Fonseca, Phys. Rev. C **75**, 014005 (2007).

[6] J. Fujita and H. Miyazawa, Prog. Theor. Phys. **17**, 360 (1957).

[7] M. Baldo, I. Bombaci, and G. F. Burgio, Astron. Astrophys. **328**, 274 (1997).

[8] A. Lejeune, U. Lombardo, and W. Zuo, Phys. Lett. B **477**, 45 (2000).

[9] M. Buenerd, P. Martin, R. Bertholet *et al.*, Phys. Rev. C **26**, 1299 (1982).

[10] M. Buenerd, J. Pinston, J. Cole *et al.*, Phys. Lett. B **102**, 242 (1981).

[11] M. Buenerd, A. Lounis, J. Chauvin *et al.*, Nucl. Phys. A **424**, 313 (1984).

[12] M. E. Brandan and G. R. Satchler, Phys. Rep. **285**, 143 (1997).

[13] T. Furumoto, Y. Sakuragi, and Y. Yamamoto, Phys. Rev. C **78**, 044610 (2008).

[14] S. Rafi, M. Sharma, D. Pachouri, W. Haider, and Y. K. Gambhir, Phys. Rev. C **87**, 014003 (2013).

[15] M. Toyokawa, M. Yahiro, T. Matsumoto, K. Minomo, K. Ogata, and M. Kohno, Phys. Rev. C **92**, 024618 (2015).

[16] T. Furumoto, Y. Sakuragi, and Y. Yamamoto, Phys. Rev. C **80**, 044614 (2009).

[17] T. Furumoto, Y. Sakuragi, and Y. Yamamoto, Phys. Rev. C **79**, 011601(R) (2009).

[18] T. Furumoto, Y. Sakuragi, and Y. Yamamoto, Phys. Rev. C **82**, 044612 (2010).

[19] K. Minomo, M. Toyokawa, M. Kohno, and M. Yahiro, Phys. Rev. C **90**, 051601(R) (2014).

[20] K. Minomo, M. Kohno, and K. Ogata, Phys. Rev. C **93**, 014607 (2016).

[21] W. W. Qu, G. L. Zhang, S. Terashima *et al.*, Phys. Lett. B **751**, 1 (2015).

[22] T. Furumoto, Y. Sakuragi, and Y. Yamamoto, Phys. Rev. C **90**, 041601(R) (2014).

[23] T. Furumoto, Y. Sakuragi, and Y. Yamamoto, Phys. Rev. C **94**, 044620 (2016).

[24] J. Y. Hostachy *et al.*, Nucl. Phys. A **490**, 441 (1988).

[25] T. Ichihara *et al.*, Nucl. Phys. A **569**, 287 (1994).

[26] Y. Yamamoto, T. Furumoto, N. Yasutake, and Th. A. Rijken, Phys. Rev. C **90**, 045805 (2014).

[27] Y. Yamamoto, T. Furumoto, N. Yasutake, and T. A. Rijken, Eur. Phys. J. A **52**, 19 (2016).

[28] K. Hatanaka, K. Takahisa, H. Tamura *et al.*, Nucl. Instrum. Methods Phys. Res., Sect. A **384**, 575 (1997).

[29] A. Tamii, Y. Fujita, H. Matsubara *et al.*, Nucl. Instrum. Methods Phys. Res., Sect. A **605**, 326 (2009).

[30] T. Wakasa *et al.*, Nucl. Instrum. Methods Phys. Res., Sect. A **482**, 79 (2002).

[31] W. W. Qu *et al.*, Chin. Phys. C **38**, 116202 (2014).

[32] M. Fujiwara, H. Akimune, and I. Daito *et al.*, Nucl. Instrum. Methods Phys. Res., Sect. A **422**, 484 (1999).

[33] K. Strauch and F. Titus, Phys. Rev. **103**, 200 (1953).

[34] W. W. Qu, G. L. Zhang, and S. Terashima *et al.*, Nucl. Sci. Tech. **25**, 050501 (2014).

[35] M. Itoh, H. Akimune, M. Fujiwara, U. Garg, N. Hashimoto, T. Kawabata, K. Kawase, S. Kishi, T. Murakami, K. Nakanishi, Y. Nakatsugawa, B. K. Nayak, S. Okumura, H. Sakaguchi, H. Takeda, S. Terashima, M. Uchida, Y. Yasuda, M. Yosoi, and J. Zenihiro, Phys. Rev. C **84**, 054308 (2011).

[36] F. Coester, S. Cohen, B. D. Day *et al.*, Phys. Rev. C **1**, 769 (1970).

[37] T. A. Rijken, Phys. Rev. C **73**, 044007 (2006).

[38] T. A. Rijken and Y. Yamamoto, Phys. Rev. C **73**, 044008 (2006).

[39] M. M. Nagels, T. A. Rijken, and Y. Yamamoto, arXiv:1408.4825.

[40] M. M. Nagels, T. A. Rijken, and Y. Yamamoto, arXiv:1501.06636.

[41] T. Kasahara, Y. Akaishi, and H. Tanaka, Prog. Theor. Phys. Suppl. **56**, 96 (1974).

[42] T. Furumoto, W. Horiuchi, M. Takashina, Y. Yamamoto, and Y. Sakuragi, Phys. Rev. C **85**, 044607 (2012).
[43] T. Furumoto and Y. Sakuragi, Phys. Rev. C **87**, 014618 (2013).
[44] Y. Yamamoto, T. Furumoto, N. Yasutake, and T. A. Rijken, Phys. Rev. C **88**, 022801(R) (2013).
[45] G. R. Satchler, *Direct Nuclear Reactions* (Oxford University Press, New York, 1983).
[46] J. W. Negele and D. M. Vautherin, Phys. Rev. C **5**, 1472 (1972).
[47] F. A. Brieva and J. R. Rook, Nucl. Phys. A **291**, 299 (1977).
[48] F. A. Brieva and J. R. Rook, Nucl. Phys. A **291**, 317 (1977).
[49] F. A. Brieva and J. R. Rook, Nucl. Phys. A **297**, 206 (1978).
[50] M. Kamimura, Nucl. Phys. A **351**, 456 (1981).
[51] M. Takechi, M. Fukuda, M. Mihara *et al.*, Phys. Rev. C **79**, 061601(R) (2009).
[52] F. D. Smit, F. Nemulodi, and Z. Buthelezi *et al.*, Phys. Rev. C **86**, 037301 (2012).
[53] F. Perey and G. R. Satchler, Phys. Lett. **5**, 212 (1963).